Stagnation enthalpy effects on hypersonic turbulent compression corner flow at moderate Reynolds numbers

M. Di Renzo [*]

Department of Engineering for Innovation, University of Salento, Lecce 73100, Italy
and Center for Turbulence Research, Stanford University, Stanford, California 94305, USA

C. T. Williams

Center for Turbulence Research, Stanford University, Stanford, California 94305, USA

S. Pirozzoli

Department of Mechanical and Aeronautical Engineering, Sapienza University of Rome, Rome 00183, Italy

The effects of stagnation enthalpy on a hypersonic boundary layer developing over a compression ramp are analyzed in this work using direct numerical simulations. Separate sets of simulations with different values of free-stream temperature, wall-cooling rate, and edge Mach number are carried out to evaluate and isolate stagnation enthalpy effects. Moreover, these sets of calculations are performed with and without vibrational excitation to further characterize the impact of this thermodynamic phenomenon on the flow. The presented calculations show that the variation of stagnation enthalpy and the presence of vibrational excitation are not able to qualitatively alter the structure of the flow. From a quantitative point of view, it is shown that the variation of the thermodynamic state of the gas can cause a 10% variation in the skin-friction coefficient, a 20% decrease in wall heat flux, and a shift in the typical frequencies of wall-pressure fluctuations by a factor of 2 toward higher frequencies.

I. INTRODUCTION

Aircraft that fly at hypersonic Mach numbers and low altitudes experience intense mechanical and thermal loads on their surface [1–3]. In particular, when the Reynolds number of the flow surrounding the fuselage is sufficiently high to trigger the transition to turbulence, strongly nonlinear interaction of complex thermochemical effects with transport phenomena due to the high velocity of the gas is activated [1,4]. The correct prediction of these fundamental phenomena is of primary importance to achieve a precise evaluation of the thermal and mechanical loads of hypersonic aerospace applications.

Significant advances in describing the behavior of wall-bounded compressible, and more specifically, hypersonic turbulence have been achieved in the past years in the context of low-enthalpy flows. These flows are characterized by low stagnation temperatures, which most of the time imply cryogenic static temperatures in the free stream and prevent the activation of vibrational excitation, chemical dissociation, and thermochemical nonequilibrium. Most of the efforts are related to boundary layers developing on flat plates in supersonic [5,6] and hypersonic [7–11] regimes. The

---

[*]Corresponding author: mario.direnzo@unisalento.it

main objective of these studies was to assess the importance of compressibility and wall heat transfer on the dynamics of the boundary layer. Specifically, various transformations that attempt to map the mean compressible flow onto its incompressible counterpart have been formulated and tested with mixed results, depending on the edge Mach number of the flow and the intensity of the wall heat flux [12–14]. Similarly, several decompositions of the skin friction and wall heat flux have been proposed to highlight how the various hydrodynamic phenomena occurring in the boundary layer influence the exchange of energy and momentum with the solid wall [15,16]. Interactions of compressible boundary layers with oblique shocks have also been investigated considering configurations where either the compression wave is generated by external shock generators [17,18] or by a compression corner [19,20]. A main point of interest in these studies is the quantification and modeling of low-frequency unsteadiness of the wall pressure field [21,22]. In fact, it is known that the hydrodynamic fluctuations of the preshock boundary layer coupled with the separation bubble formed by the flow separation at the shock foot generate very-low-frequency oscillations of the pressure field that might be dangerous for the structural integrity of hypersonic vehicles.

The higher computational complexity associated with considering high-enthalpy effects has limited studies of turbulent flows where vibrational excitation, chemical equilibrium, and thermal nonequilibrium are active. Recently, spatially evolving boundary layers with stagnation enthalpies of the order of tens of megajoule per kilogram have been computationally analyzed considering chemical [23] and thermochemical nonequilibrium [24]. These studies have highlighted the importance of turbulent transport on the atomic species distribution within the boundary layer and the high-turbulence–chemistry interaction achieved in flows of this kind. Very recently, high-enthalpy effects have also been investigated in the context of oblique shocks impinging on transitional boundary layers [25]. Further characterization of these phenomena in the context of turbulent compression corners still requires investigation.

The present study analyzes the effects of stagnation enthalpy on hypersonic compression corner flow. Direct numerical simulations (DNS) of a fully turbulent compression corner flow are carried out for different wall-cooling ratios, free-stream Mach numbers, and stagnation enthalpies considering the vibrational excitation of the gas. The rest of the manuscript is organized as follows. Section II describes the mathematical and numerical formulation utilized to carry out the presented simulations and the computational setup. The main results of the simulations are presented in Sec. III, where the analysis is focused mainly on integral quantities of engineering interest, such as the skin-friction coefficient, the heat flux at the wall, and the intensity of the wall-pressure fluctuations. Lastly, conclusions are given in Sec. IV.

II. MATHEMATICAL FORMULATION

The DNS presented in this work have been carried out using the Hypersonic Task-based Research (HTR) solver [26–28]. HTR is a compressible Navier–Stokes solver capable of executing large-scale simulations of compressible reacting flows, taking into account multicomponent transport and finite-rate chemistry. Specifically, the presented results are obtained by solving the conservation equations of mass, momentum, and energy, namely,

$$\frac{\partial \rho}{\partial t} + \nabla \cdot (\rho \mathbf{u}) = 0, \tag{1}$$

$$\frac{\partial (\rho \mathbf{u})}{\partial t} + \nabla \cdot (\rho \mathbf{u}\mathbf{u}) = -\nabla P + \nabla \cdot \overline{\overline{\tau}}, \tag{2}$$

$$\frac{\partial (\rho e_0)}{\partial t} + \nabla \cdot (\rho \mathbf{u} h_0) = \nabla \cdot (\lambda \nabla T + \overline{\overline{\tau}} \mathbf{u}). \tag{3}$$

In this formulation, t is the time coordinate, ρ is the density, $\mathbf{u}$ is the velocity vector, P is the thermodynamic pressure, and T is the temperature of the gas. The viscous stress tensor $\overline{\overline{\tau}}$ is defined

as

$$\overline{\overline{\tau}} = \mu[\nabla \mathbf{u} + \nabla \mathbf{u}^T - 2(\nabla \cdot \mathbf{u})\overline{\overline{I}}/3], \tag{4}$$

where $\overline{\overline{I}}$ is the identity tensor, and the viscosity of the fluid is determined as a function of the local temperature using Sutherland's law: $\mu = \mu_{\text{ref}}(T/T_{\text{ref}})^{\frac{3}{2}}(T_{\text{ref}} + S)/(T + S)$. In particular, $T_{\text{ref}} = 271.15$ K and $S = 110.4$ K have been selected in order to reproduce the behavior of standard air. The formulation is supplemented with the ideal-gas equation of state $P = \rho R_g T$, where R_g is the gas constant.

In Eq. (3), $e_0 = e + |\mathbf{u}|^2/2$ and $h_0 = e_0 + P/\rho$ are the specific values of the stagnation internal energy and enthalpy, respectively. In this formulation, e is the specific internal energy that is computed as a function of temperature with the expression

$$e = h_r + \int_{T_r}^{T} c_p dT' - \frac{P}{\rho}, \tag{5}$$

where c_p is the constant-pressure specific heat capacity, and h_r is a reference enthalpy evaluated at the corresponding temperature T_r.

In this work, two types of gas in thermodynamic equilibrium are considered, using (a) a diatomic calorically perfect gas (CPG) model, for which $T_r = 0$, $h_{\text{ref}} = 0$, and $c_p = 7R_g/2$, and (b) a calorically imperfect gas (CIG) with the same value of R_g but whose specific heat capacity and specific enthalpies are computed as functions of the local temperature using the nine-coefficient NASA polynomials particularized for a gas mixture composed of 79% N_2 and 21% O_2 on a molar basis [29]. In both cases, the thermal conductivity of the gas, λ, is computed as a function of the local viscosity and specific heat capacity at constant pressure with a constant Prandtl number assumption, namely, $\text{Pr} = c_p \mu/\lambda = 0.71$.

The conservation equations are discretized over a curvilinear computational grid using a conservative formulation [30]. In particular, the Euler fluxes are discretized with a sixth-order centered hybrid scheme, whereby a sixth-order skew-symmetric formulation that preserves kinetic energy [31] is utilized in the smooth regions of the flow and a targeted essentially nonoscillatory (TENO) scheme [32] is used for stencils that are crossed by discontinuities. The smoothness of the flow is measured direction-by-direction using a shock sensor based on the TENO6-A smoothness factors, where the cutoff parameter adaptation is based on a Ducros sensor [33]. The viscous fluxes are discretized in divergence form using a second-order centered scheme. The resulting set of ordinary differential equations is advanced in time using a Runge–Kutta strong-stability-preserving third-order scheme [34]. Further details about the numerical procedures utilized in this work, along with performance analyses of test benchmark cases, can be found in Di Renzo *et al.* [26].

A. Computational setup and flow parameters

The computational setup considered in this study consists of the prismatic domain sketched in Fig. 1. A $15°$ compression corner is located at the origin of the system of coordinates. A hypersonic turbulent boundary layer of thickness δ_0 is injected through the inflow boundary. The free stream of the incoming boundary layer has a velocity U_e, temperature T_e, and density ρ_e. The distance between the left surface of the domain and the compression corner is equal to $L_1 = 60\delta_0$. The turbulence in the injected boundary layer is sustained using a recycle-rescaling boundary condition, which samples the velocity and temperature fluctuations on a plane located $40\delta_0$ downstream of the inlet plane [35].

The wall along the compression corner is kept at a constant temperature T_w and its shape is defined by the equation $y_w(x) = d_2[f(x) - f(-60)]$, where $f(x) = x + \log[\cosh(xd_1)]/d_1$, $d_1 = (1 + d_2^2)^{\frac{3}{2}}/R_c$, and $R_c = 0.05\delta_0$ is the radius of curvature of the compression corner, imposed to avoid any discontinuity in the computational grid metrics, while d_2 is numerically determined to guarantee the correct deflection angle.
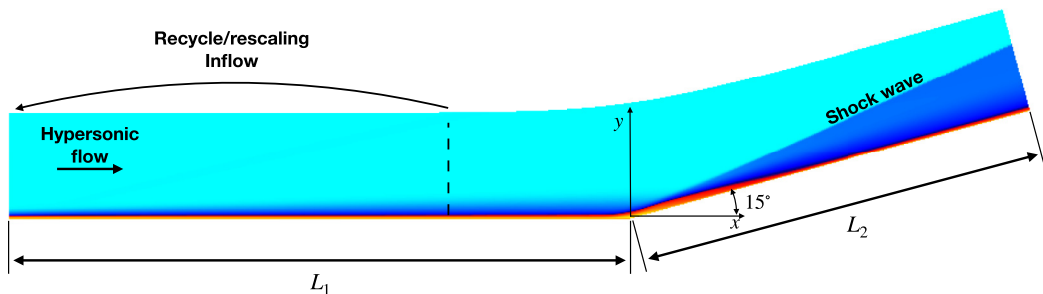
FIG. 1. Schematics of the computational setup. The contour plot shown in the figure corresponds to one of the computed average temperature fields.

The top surface of the computational domain is located $10\delta_0$ units above the wall, while its shape is represented by a mathematical expression similar to the bottom wall with $R_c = 10\delta_0$. The boundary condition along the top surface is treated with a characteristic far-field boundary condition that switches between a characteristics-based outflow (if the local flow exits the surface) and a nonreflective inflow that weakly imposes the free-stream conditions (if the flow locally enters the computational domain).

The right surface of the computational domain is positioned $L_2 = 40\delta_0$ downstream of the compression corner and is modeled using a nonreflective outflow [36]. The computational domain is $10\delta_0$ wide in the z direction normal to the sketch, along which periodicity is enforced.

The computational grid is uniform along the periodic direction and is stretched with a hyperbolic sine function in the wall-normal direction to achieve a grid spacing that is similar to unity in local friction (plus) units for the entire computational domain. Approximately 30% of the grid points assigned to the streamwise direction are uniformly distributed in the region of the computational domain upstream of the interaction, whereas the rest of the points are smoothly clustered downstream of the compression corner to achieve an approximately uniform grid resolution normalized in local friction units. In particular, the positions of the grid points in the x direction are determined as $x_i = [L_1 + L_2 \cos(15°)][g(\xi - r_p) - g(-r_p)] - L_1$, where the normalized grid index $\xi = i/(N_x - 1)$ is a parameter that is zero for the first point of the computational grid ($i = 0$) and one at the last point ($i = N_x - 1$). N_x is the number of computational grid points utilized along the streamwise direction, and $g(x)$ is a stretching function defined as

$$g(x) = \frac{L_1}{r_p[L_1 + L_2 \cos(15°)]}x - c_2[f(\xi - r_p) - f(-r_p)], \qquad (6)$$

where r_p is the parameter that controls the clustering, and c_2 is a constant numerically determined in order to obtain a computational grid of the correct size. The results shown below correspond to nine cases whose main parameters are summarized in Table I. The subscripts e and w mean that the quantity is evaluated at the edge of the incoming boundary layer and at the wall, respectively. These simulations differ mainly with respect to the thermodynamic state of the free stream, the edge Mach number of the incoming boundary layer, the dimensionless temperature of the wall, and the thermodynamic model that describes the gas. In general, we can divide the presented calculations into three sets composed of three calculations.

Within each set of calculations, the configurations with $T_{\text{ref}}/T_e = 2.7315$ are at low-enthalpy conditions ($T_e = 100$ K) and are representative of the state of the art for DNS of hypersonic compression ramps. The setups at $T_{\text{ref}}/T_e = 0.5463$ ($T_e = 500$ K) have higher stagnation enthalpy, and they reach thermodynamic states that activate vibrational excitation within the boundary layer. For this reason, these simulations are carried out with both the CPG and CIG models. In this way, the influence of the variation of the viscosity field on the flow is highlighted by comparing the high- and low-enthalpy CPG simulations, whereas the effects of vibrational excitation are

TABLE I. Setup parameters of the presented simulations where M_e is the edge Mach number at the inlet, $Re_0 = \rho_e U_e \delta_0 / \mu_e$ is the Reynolds number computed at the inlet with the edge conditions, N_x, N_y, and N_z are the number of grid points along the Cartesian directions.

Label	Model	Ma_e	T_w/T_e	T_{ref}/T_e	h_w/h_{aw}	T_w/T_{aw}	Re_0	$N_x \times N_y \times N_z$	r_p
M5_T22_loH_CPG	CPG	5	2.2	2.731	0.400	0.400	1.0×10^4	$2560 \times 450 \times 768$	0.35
M5_T22_hiH_CPG	CPG	5	2.2	0.546	0.400	0.400	1.0×10^4	$3000 \times 450 \times 1024$	0.35
M5_T22_hiH_CIG	CIG	5	2.2	0.546	0.355	0.462	1.0×10^4	$3000 \times 450 \times 1024$	0.30
M5_T33_loH_CPG	CPG	5	3.3	2.731	0.600	0.600	1.2×10^4	$2560 \times 256 \times 620$	0.30
M5_T33_hiH_CPG	CPG	5	3.3	0.546	0.600	0.600	1.2×10^4	$2560 \times 256 \times 810$	0.30
M5_T33_hiH_CIG	CIG	5	3.3	0.546	0.625	0.693	1.2×10^4	$2560 \times 256 \times 810$	0.30
M6_T45_loH_CPG	CPG	6	4.5	2.731	0.600	0.600	1.4×10^4	$2240 \times 256 \times 600$	0.25
M6_T45_hiH_CPG	CPG	6	4.5	0.546	0.600	0.600	1.4×10^4	$2688 \times 256 \times 768$	0.25
M6_T45_hiH_CIG	CIG	6	4.5	0.546	0.663	0.714	1.4×10^4	$2688 \times 256 \times 768$	0.25

observed while comparing the two high-enthalpy simulations with different thermodynamic models. The high-enthalpy free-stream static temperature considered in this study has been selected to generate a stagnation enthalpy between 3 and 4 MJ, which is similar to that experienced by many hypersonic systems flown in the past [37]. Moreover, in the considered thermodynamic conditions, the activation of vibrational excitation in the inviscid region of the flow is marginal both upstream and downstream of the oblique shock wave emanated by the compression corner. Thus the intensities of the shock waves are very similar in all the calculations at equal Mach numbers.

Two sets of cases contain configurations with $M_e = 5$ and with different wall-cooling rates. In particular, the first set of calculations, which is composed of the cases M5_T22_loH_CPG, M5_T22_hiH_CPG, and M5_T22_hiH_CIG, has an intense wall cooling, namely, $T_w/T_e = 2.2$. The second set of calculations, which is composed of the cases M5_T33_loH_CPG, M5_T33_hiH_CPG, and M5_T33_hiH_CIG, has a milder cooling, namely, $T_w/T_e = 3.3$. These two different sets of calculations are analyzed to define the effects of wall cooling on the flows at Mach 5. A third set of calculations, with a higher Mach number, namely, $M_e = 6$, has been included in the analysis to assess the effects of M_e on the flow. The wall temperature for this set of cases has been selected to produce a mild wall-cooling similar to the M5_T33 calculations. In fact, both these sets of calculations have a ratio between the wall enthalpy and the adiabatic wall enthalpy, $h_{aw} = h_e + rU_e^2/2$, which is about 0.6. In the adiabatic-wall-enthalpy expression, $r = 0.9$ is the recovery factor that here is assumed to be constant regardless of the thermodynamic state of the gas. The influence of high-enthalpy effects on the recovery factor of a boundary layer has never been rigorously quantified; therefore the validity of this assumption will need to be further investigated in the future.

It is noteworthy that for the CIG simulations, the ratio h_w/h_{aw} changes nonlinearly with the wall temperature. In fact, while the adiabatic wall enthalpy is constant regardless of the thermodynamic model, h_w is a nonlinear function of the wall temperature for the CIG. For this reason, the ratio h_w/h_{aw} in CIG is lower (higher) than the corresponding CPG cases for the higher (lower) wall temperature. Moreover, if an approximate adiabatic wall temperature T_{aw} is computed as the temperature corresponding to h_{aw}, it appears that not even the ratio between T_w and T_{aw} is matched between the CPG and CIG cases. As a consequence, the wall-cooling rate will be only approximately matched between each CIG and corresponding CPG calculations. Table II reports some of the characteristic parameters of the presented calculations. In particular, it shows that all the considered boundary layers have similar properties upstream of the interaction ($x = -10$), whereby the Reynolds number $Re_{\delta_2} = \rho_e U_e \theta / \mu_w \sim 500$ and the friction Mach number $M_\tau = \tau_w / a_w \sim 0.16$. In the previous expressions, θ is the local momentum thickness of the boundary layer and a_w is the speed of sound computed at the wall. The table contains also the values of the computational grid spacing normalized in friction units Δ_i^+. Note that all the reported values, both upstream and

TABLE II. Main solution parameters of the presented simulations where $\mathrm{Re}_{\delta_2} = \rho_e U_e \theta / \mu_w$ is the Reynolds number based on the momentum thickness θ and the viscosity at the wall, $M_\tau = \tau_w / a_w$ is the friction Mach number, $H = \delta^*/\theta$ is the shape factor, Δ_x^+, Δ_y^+, and Δ_z^+ are the grid spacing at the wall in the streamwise, wall-normal, and spanwise directions. The superscripts up and dw mean that the quantity is computed upstream ($x = -10\delta_0$) or downstream ($x = 30\delta_0$) of the interaction, respectively.

Label	$\mathrm{Re}_{\delta_2}^{\mathrm{up}}$	M_τ^{up}	$\mathrm{Re}_\tau^{\mathrm{up}}$	H^{up}	$\Delta_x^{+\,\mathrm{up}}$	$\Delta_y^{+\,\mathrm{up}}$	$\Delta_z^{+\,\mathrm{up}}$	$\Delta_x^{+\,\mathrm{dw}}$	$\Delta_y^{+\,\mathrm{dw}}$	$\Delta_z^{+\,\mathrm{dw}}$
M5_T22_loH_CPG	525	0.164	285	7.97	6.85	0.35	1.36	9.76	1.35	5.28
M5_T22_hiH_CPG	636	0.158	336	7.90	7.13	0.35	1.24	10.18	1.35	4.85
M5_T22_hiH_CIG	646	0.165	340	7.60	8.50	0.36	1.27	9.58	1.37	4.91
M5_T33_loH_CPG	414	0.157	201	9.64	5.45	0.36	1.14	6.27	1.39	4.53
M5_T33_hiH_CPG	543	0.150	253	9.47	7.18	0.36	1.15	8.28	1.40	4.58
M5_T33_hiH_CIG	548	0.157	254	9.31	7.27	0.37	1.17	8.34	1.41	4.61
M6_T45_loH_CPG	314	0.171	152	13.65	5.35	0.26	0.84	6.17	1.31	4.32
M6_T45_hiH_CPG	430	0.163	196	13.42	6.27	0.27	0.92	7.14	1.32	4.69
M6_T45_hiH_CIG	436	0.172	204	13.06	6.36	0.27	0.94	7.20	1.33	4.72

downstream of the compression corner, are well within the DNS range, and together with the low-dissipation numerics deployed in these calculations, warrant an accurate numerical solution to the shock wave and turbulence interaction problem under consideration.

III. RESULTS

The numerical results presented in this section are collected after ten flow residence times based on the edge velocity and the length of the computational domain. Statistics are computed for an additional ten flow residence times for convergence. In the formulation employed below, the overline symbol indicates a Reynolds average, or equivalently, an unweighted average along both time and the spanwise direction. On the other hand, the tilde symbol denotes density-weighted averages, which for a generic quantity ϕ are defined as $\widetilde{\phi} = \overline{\rho\phi}/\overline{\rho}$. The prime and double prime superscripts identify the fluctuations of the quantity around the unweighted and density-weighted averages, respectively. That is, using again the generic quantity ϕ, the fluctuations around the Reynolds average are defined as $\phi' = \phi - \overline{\phi}$, while the Favre fluctuations are defined as $\phi'' = \phi - \widetilde{\phi}$.

A. Properties of the preshock turbulent boundary layer

Considering that the properties of the shock wave and turbulent-boundary-layer interaction (SBLI) ultimately depend on the conditions of the boundary layer upstream of the compression corner, this section provides a quantitative analysis of the state of the preshock flows under consideration. Figure 2 shows the streamwise velocity profiles extracted in the discussed calculations at $x = -10\delta_0$. The presented profiles are transformed using the velocity transformations proposed by van Driest [38], Trettel and Larsson [12], and Griffin *et al.* [14]. For all transformations and all considered sets of conditions, the most significant differences among the profiles are observed between the high-enthalpy conditions, regardless of the considered gas model, and the low-enthalpy cases. The profiles of the van Driest transformed velocity u_{VD} are plotted against the wall-normal distance normalized in friction units and provide the worst agreement with the incompressible law of the wall. The u_{VD} falls below the linear scaling in the near-wall region while overpredicting the logarithmic region, namely, $u_{VD} = \ln(y^+)/0.41 + 5.2$. This gap in the near-wall region depends on the wall cooling, as observed in previous studies [10]. As expected, the gap between u_{VD} and the linear scaling is more significant for the Mach-5 cases with stronger wall cooling than in the cases with warmer walls. Conversely, the upward shift of the logarithmic layer depends on the Mach number of the flow, with the Mach-5 cases being closer to the reference scaling. The van
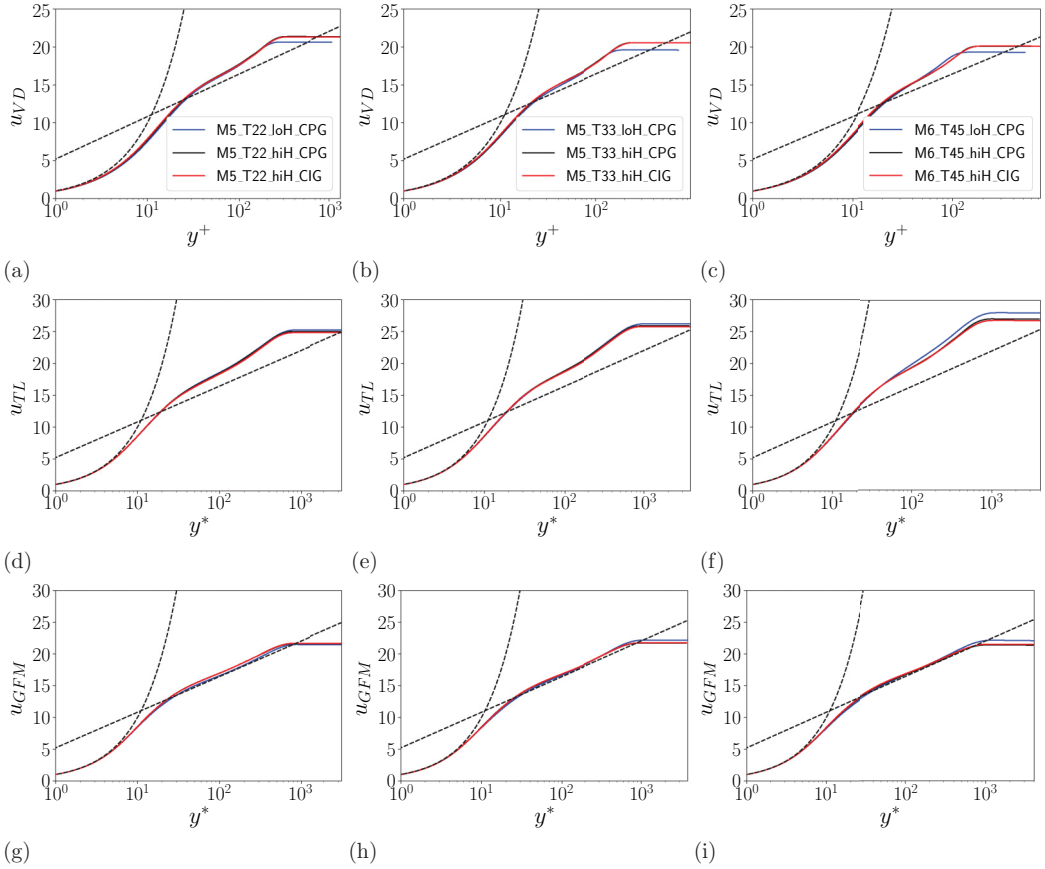
FIG. 2. (a)–(c) van Driest, (d)–(f) Trettel-Larsson, and (h)–(i) Griffin-Fu-Moin transformed mean velocity profiles of the preshock boundary layer ($x = -10\delta_0$) for the cases (a), (d), (g) $M_e = 5$ and $T_w/T_e = 2.2$, (b), (e), (h) $M_e = 5$ and $T_w/T_e = 3.3$, and (c), (f), (i) $M_e = 6$ and $T_w/T_e = 4.5$. The dashed lines represent the incompressible wall law for reference.

Driest transformation provides an overall good collapse between each set of cases, with the larger differences observed in the wake of the low-enthalpy CPG calculations, which is shifted downward with respect to the high-enthalpy cases.

The use of the semilocal coordinate, $y^* = y\mu/\sqrt{\rho\tau_w}$, where τ_w is the local average wall-shear stress developed by the flow in the streamwise direction, in plotting the Trettel-Larsson (u_{TL}) and Griffin-Fu-Moin (u_{GFM}) transformed velocity profiles appears to be crucial for achieving a linear scaling of the velocity profiles in the near-wall region regardless of the wall-cooling, free-stream stagnation enthalpy, and gas thermodynamic model. The Trettel-Larsson transformation provides a good collapse of the different calculations in the Mach-5 conditions. At the same time, it shows a slight upward shift of the Mach-6 low-enthalpy velocity profile with respect to the higher enthalpy cases. For all the flow conditions included in the present study, the logarithmic layer of the velocity profiles is characterized by higher velocities as compared to the incompressible logarithmic law. On the other hand, the Griffin-Fu-Moin transformation yields the best collapse of all thermodynamic conditions with the law of the wall. The only minor differences observed for the u_{GFM} profiles are located in the wake of Figs. 2(h) and 2(i), for which the low-enthalpy velocity profile has higher transformed free-stream velocities. Figure 3 shows the components of the turbulent stress tensor normalized by the local wall-shear stress and plotted versus the wallnormal coordinate in semilocal
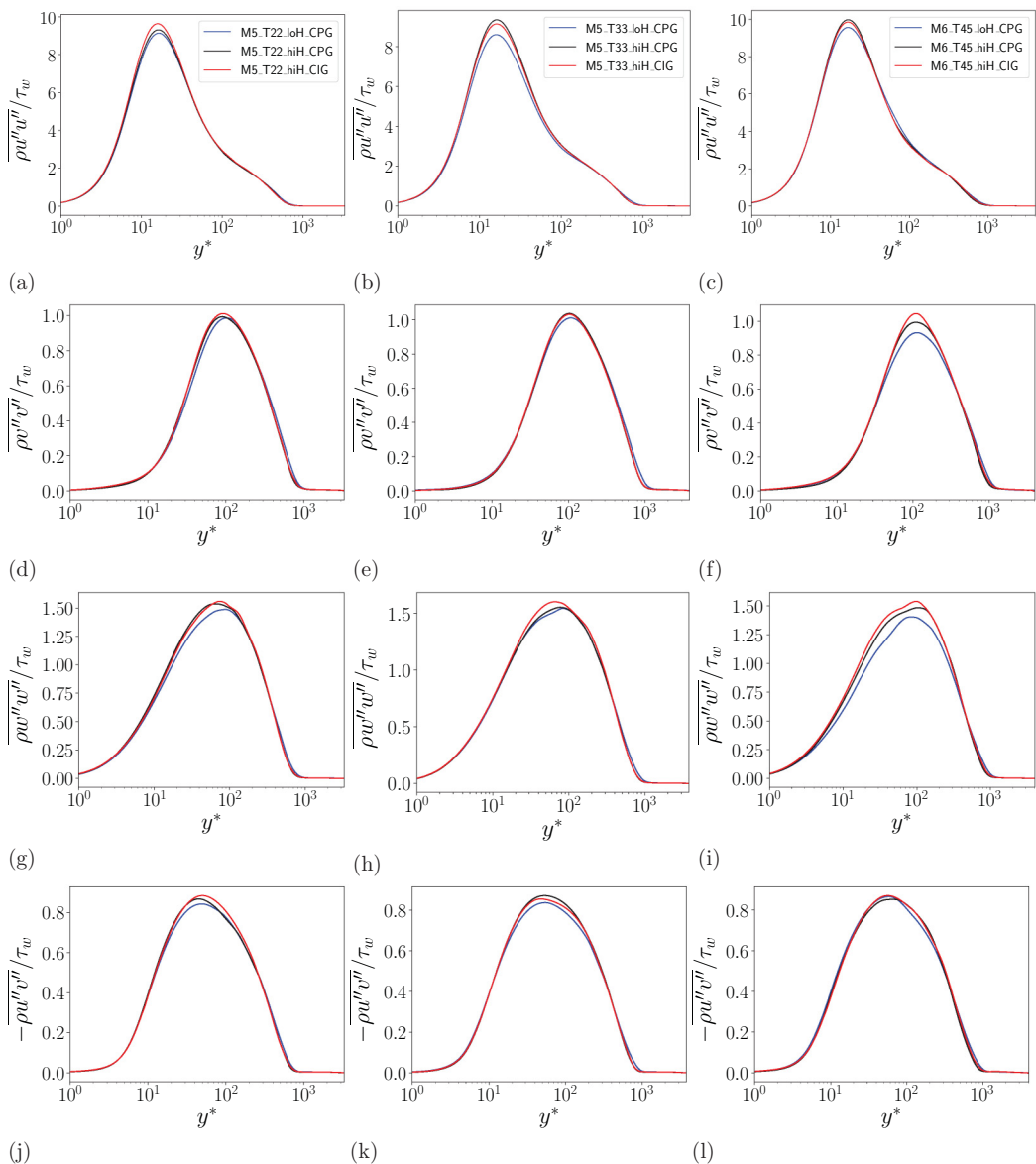
FIG. 3. Normalized turbulent stress profiles of the preshock boundary layer ($x = -10\delta_0$) for the cases (a), (d), (g), (j) $M_e = 5$ and $T_w/T_e = 2.2$, (b), (e), (h), (k) $M_e = 5$ and $T_w/T_e = 3.3$, and (c), (f), (i), (l) $M_e = 6$ and $T_w/T_e = 4.5$.

units. The profiles obtained in all the edge conditions and with both thermodynamic gas models are very similar overall. In general, the high-enthalpy cases show slightly larger normalized turbulent stresses in all the plotted components. For this reason, this increase in stresses can be mainly attributed to local Reynolds number effects. In fact, the higher T_e utilized in the high-enthalpy setups shifts the operating region of the Sutherland law, leading to a lower-viscosity rise in the peak temperature region, thus decreasing the overall Reynolds number. The vibrational excitation does not have a definite effect, as the simulations with the CIG model produce marginal increases or decreases of the turbulent stresses depending on the configuration and component of the stress
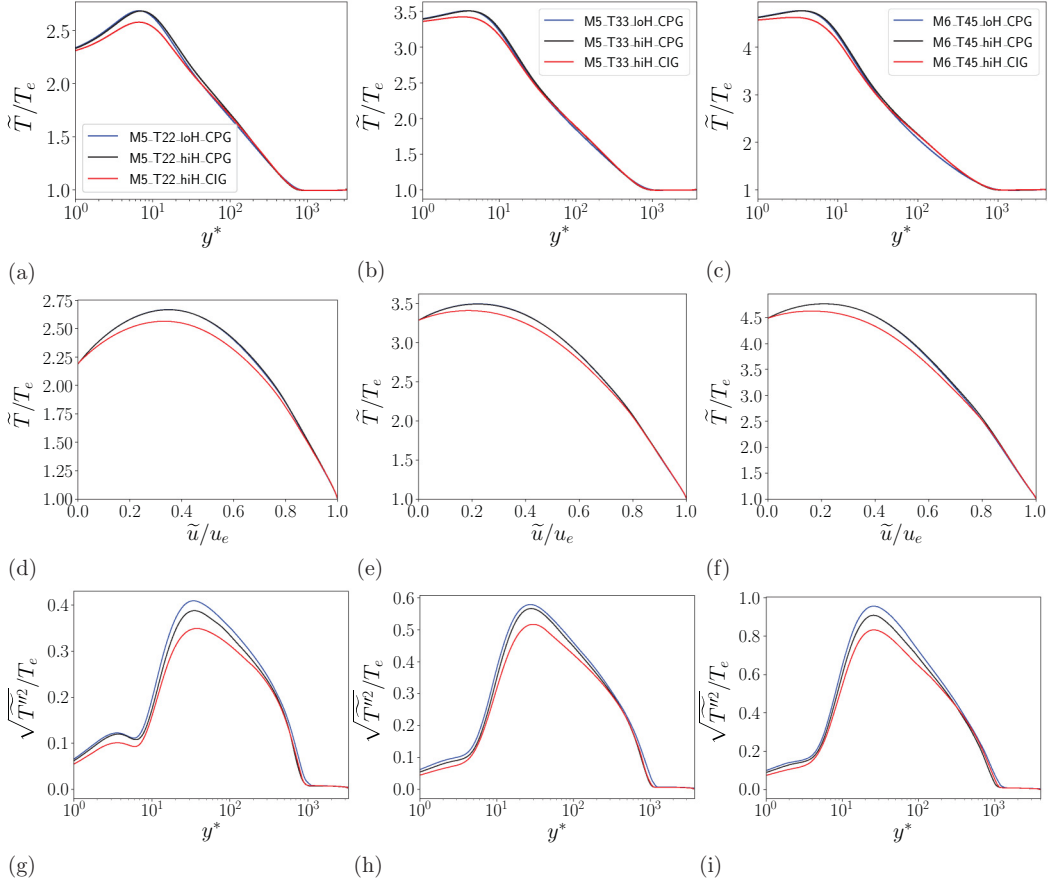
FIG. 4. Normalized mean and rms of temperature profiles of the preshock boundary layer ($x = -10\delta_0$) for the cases (a), (d), (g) $M_e = 5$ and $T_w/T_e = 2.2$, (b), (e), (h) $M_e = 5$ and $T_w/T_e = 3.3$, and (c), (f), (i) $M_e = 6$ and $T_w/T_e = 4.5$. Panels (d), (e), (f) show the relation between mean velocity and temperature within the boundary layer.

tensor that is considered. Figure 4 shows the normalized value of the Favre mean and rms of the static gas temperature. In all the considered cases, the temperature peaks at about $y^* \sim 10$, whereby the increase of internal energy due to the viscous heating is balanced by wall cooling. The stagnation enthalpy at the edge of the boundary layer does not seem to play a significant role in the distribution of the mean temperature. In fact, the low-enthalpy and high-enthalpy CPG cases overlap in all three considered conditions. Conversely, the introduction of vibrational excitation in the mixture with the CIG model induces a reduction of the maximum temperature achieved within the boundary layer. This reduction is particularly evident for the $M_e = 5$ $T_w/T_e = 2.2$ configuration, whereby the peak temperature is lowered by about 10%, but it is also present in the other cases with warmer walls. Such reduction of the temperature peak intensity is directly correlated to the reduction of the wall heat flux that will be described in Sec. III B. Figures 4(d)–4(f) show the normalized value of the density-weighted mean temperature as function of the normalized density-weighted mean streamwise velocity. This type of relation has been utilized in multiple studies to quantify the accuracy of the strong Reynolds analogy [10,39] or to construct wall models for compressible boundary layers [40]. These plots also show that the variation of the free-stream stagnation enthalpy does not directly affect the mean temperature distribution unless vibrational excitation is activated. In fact, the CIG cases show a temperature-velocity relation that is qualitatively similar to the

corresponding CPG cases but with lower mean temperatures. For this reason, the Crocco-Busemann, Walz, or Zhang [39] relations will need to be revised before they can be applied to high-enthalpy boundary layers, whereby the specific heat capacity of the gas is not constant.

The effects of the edge Mach number and stagnation enthalpy are more visible in the temperature fluctuations shown in Figs. 4(g)–4(i). The low-enthalpy CIG flows produce the most intense fluctuations in all the considered configurations. The peak of fluctuation intensities happens at around $y^* \sim 50$, where the cold gas from the outer parts of the boundary layer is mixed with the hot air produced by viscous heating close to the walls. The intensity of these fluctuations increases with the wall temperature and with the edge Mach number. The high-enthalpy flows tend to have weaker fluctuations of the static temperature; however, the gap with the low-enthalpy profiles depends on the specific boundary-layer properties. The introduction of vibrational excitation in the thermodynamic description of the gas decreases the $\widetilde{T''^2}$ for all considered configurations.

B. Distribution of skin-friction coefficient and wall heat flux

Figure 5 shows the distributions of the skin-friction coefficient $C_f = 2\tau_w/(\rho_e U_e^2)$. All the analyzed boundary layers require an adaptation length of about $20\delta_0$ downstream of the inflow. At this location, which corresponds to the inflection point in the C_f profile, the boundary-layer turbulence achieves a physically meaningful state that is not affected by the recycle-rescaling boundary condition. A small separation bubble of approximate size δ_0 is generated as a result of SBLI at the compression corner. As observed in Figs. 5(a), 5(c) and 5(e), an overall trend in the cases involving CPG away from the separation and reattachment zones is a 10% decrease in the skin-friction coefficient upon increasing the stagnation enthalpy by 400%. However, an increase in the skin-friction coefficient is observed when swapping the assumption of CPG for the CIG approximation. As a result, the aforementioned increase in stagnation enthalpy leads to only a moderate decrease of approximately 5% in the skin-friction coefficient when vibrational-excitation effects are incorporated. In contrast, as shown in Figs. 5(b), 5(d) and 5(f), the size of the separation bubble appears to remain mostly unaltered across all cases.

A variation of the stagnation enthalpy modifies significantly the flow just upstream of the separation bubble, although the bubbles themselves remain largely unaffected by the change in the thermodynamic model. In particular, the upstream influence of the SBLI, which is measured by the departure from the classical C_f scaling, is delayed by the increase in the stagnation enthalpy and by the introduction of the CIG model. These differences observed between the low- and high-enthalpy setups are to be attributed to Reynolds number and thermodynamic effects. In fact, the two CPG simulations differ only in the relation between the molecular viscosity and the local temperature. The lower enthalpy conditions experience a larger variation of viscosity across the boundary layer, leading to lower local Reynolds numbers. The additional endothermicity introduced by the CIG model reduces the magnitude of the temperature peak generated in the boundary layer, thus decreasing the maximum viscosity of the fluid and further increasing the local Reynolds number. This aspect of the presented results is also visible in the trend of the shape factors $H = \delta^*/\theta$, where δ^* is the boundary-layer displacement thickness, reported in Table II. In fact, H becomes increasingly lower when the stagnation enthalpy increases and when vibrational excitation is considered in the calculations. As higher Reynolds number boundary layers with lower shape factors are less prone to separate and the separation bubble must be located across the compression corner, the C_f profile of the higher Reynolds flow has a shorter upstream influence and steeper transition. For this reason, the increase in the stagnation enthalpy and the introduction of the CIG model steepen the C_f profiles upstream of the separation point. Moreover, the increase of the stagnation enthalpy and the introduction of vibrational excitation lower the sonic line of the preshock boundary layer toward the wall. The distance between the sonic line and the wall in the preshock region is decreased in the CIG calculations with respect to the CPG low-enthalpy cases by about 25%, 28%, and 37% in the cold-wall $M_e = 5$, warm-wall $M_e = 5$, and $M_e = 6$ configurations, respectively. The shorter extent of the subsonic region in the boundary layer contributes to reducing the upstream
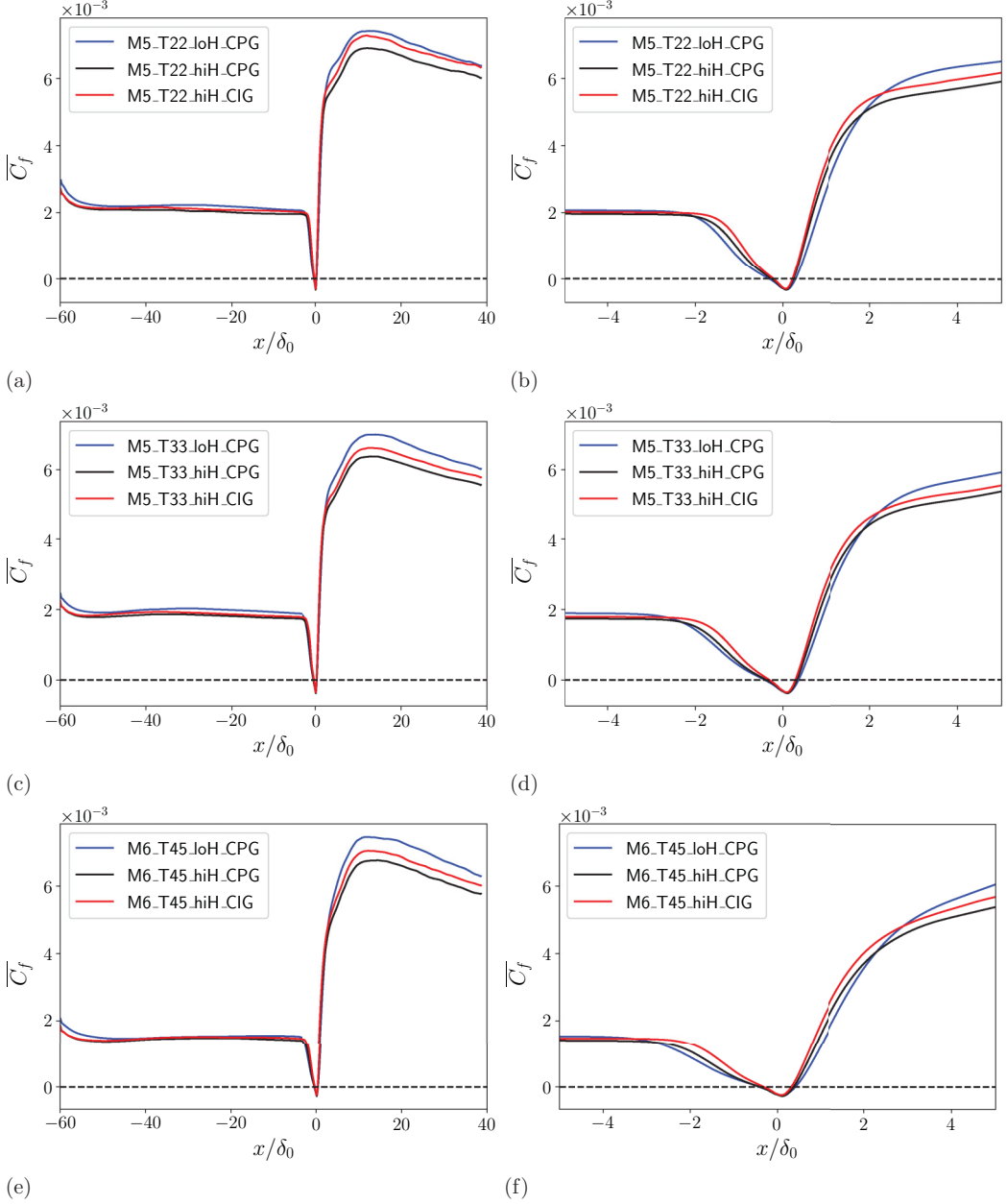
FIG. 5. Skin-friction coefficient as a function of streamwise distance for the calculations with (a) $M_e = 5$ and $T_w/T_e = 2.2$, (c) $M_e = 5$ and $T_w/T_e = 3.3$, and (e) $M_e = 6$ and $T_w/T_e = 4.5$. Panels (b), (d), and (f) are analogous to (a), (c), and (e), respectively, but they show a zoomed-in version of the results near the compression corner.

influence of the SBLI. Figure 6 shows the distribution of the wall heat flux using two different normalizations. The first is the classic Stanton number, defined as $\mathrm{St} = q_w/[\rho_e U_e (h_{aw} - h_w)]$, where q_w is the heat flux at the wall. The second normalization is based on the free-stream momentum flux, namely, $C_q = q_w/(\rho_e U_e^3)$, as proposed by White [41] specifically for hypersonic flows of CIG.
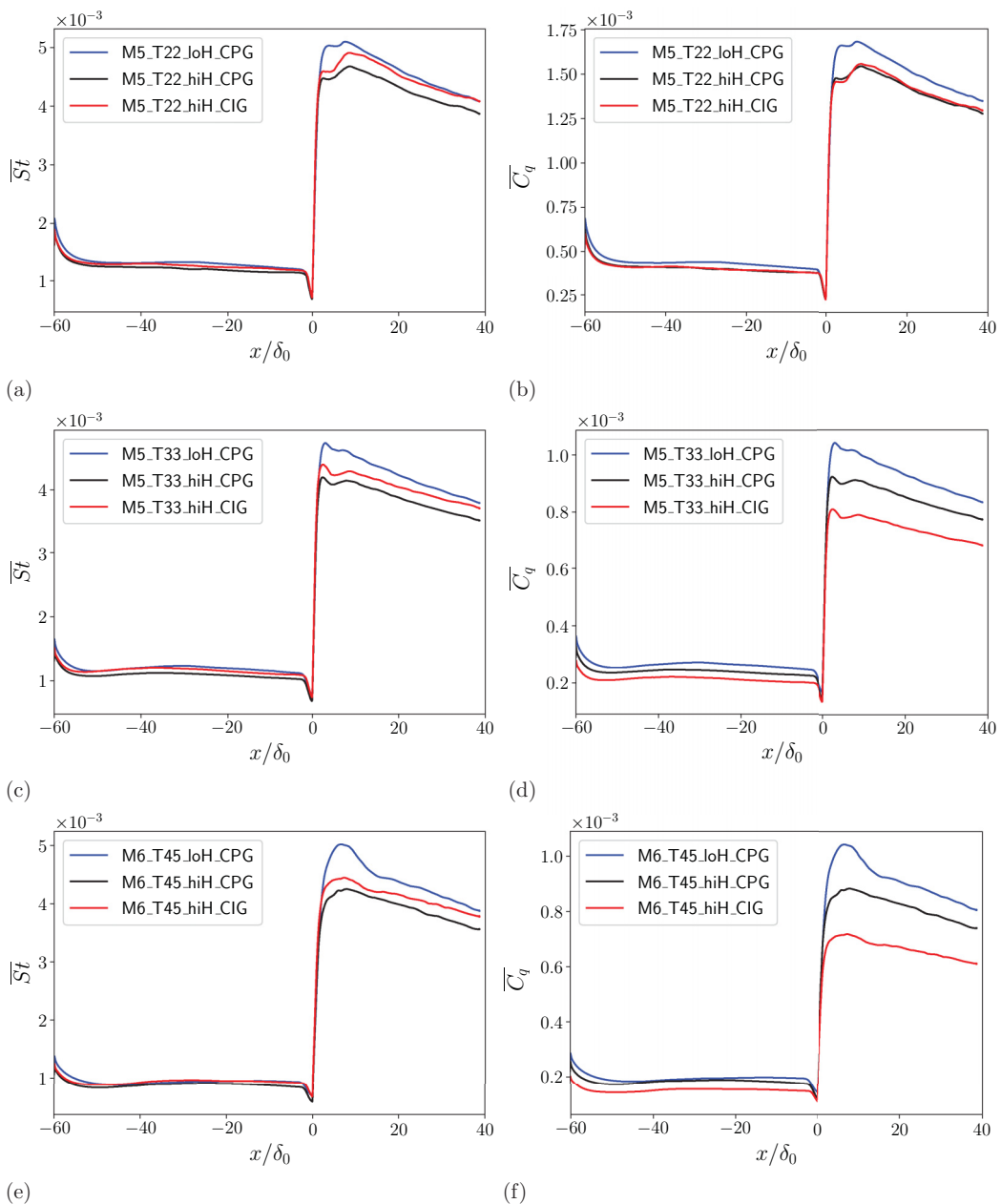
FIG. 6. Streamwise distributions of (a), (c), (e) Stanton number and (b), (d), (f) wall-heat-flux coefficient for flow cases with (a), (b) $M_e = 5$ and $T_w/T_e = 2.2$, (c), (d) $M_e = 5$ and $T_w/T_e = 3.3$, and (e), (f) $M_e = 6$ and $T_w/T_e = 4.5$.

Interestingly, the behavior of the normalized heat flux depends strongly on the chosen normalization, as a consequence of the nonlinear relationship between enthalpy and temperature in CIG. If the Stanton number distribution is considered, the effects of vibrational excitation are very similar to those observed in the skin-friction coefficient. Specifically, the highest Stanton number is found in the low-enthalpy case, whereas the high-enthalpy CPG case shows a reduction of about 10%. The
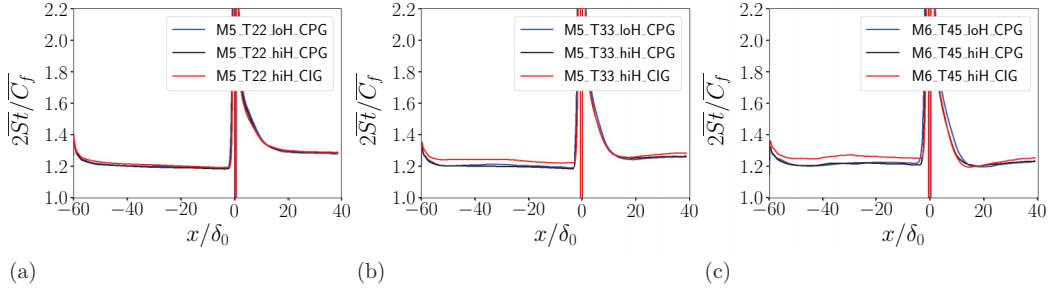
FIG. 7. Distribution along the streamwise direction of the Reynolds analogy factor for flow cases with (a) $M_e = 5$ and $T_w/T_e = 2.2$, (b) $M_e = 5$ and $T_w/T_e = 3.3$, and (c) $M_e = 6$ and $T_w/T_e = 4.5$.

CIG simulations lie in between the two CPG simulations for both wall-cooling intensities considered in this study.

If the heat-flux coefficients C_q are considered instead, a new interpretation of the CIG effects presents itself. In particular, the red curve is shifted downward in Figs. 6(b), 6(d) and 6(f). This is the effect of the endothermicity induced by vibrational excitation. As discussed in Sec. III A, the variation of the heat capacity lowers the temperature peak arising because of viscous heating. For this reason, the temperature gradients and the wall heat flux are milder. This second normalization emphasizes the reduction in the temperature gradient by vibrational excitation because the normalizing factor $\rho_e U_e^2$ is constant for the high-enthalpy CPG and CIG setups. We believe that this ambiguity in interpreting the results prompts further studies regarding the most appropriate normalization of heat fluxes in boundary layers of CIG.

The Reynolds analogy factor ($2St/C_f$) is shown in Fig. 7 for the nine calculations considered in this study. In the presented calculations, the ratio $2St/C_t$ remains remarkably independent of the wall cooling and edge Mach number. All the calculations with the CPG assumption show a Reynolds analogy faction similar to 1.2 in the upstream section of the computational domain. The values shown downstream of the compression corner, away from the separation bubble, have a more significant dependence of T_w/T_e and M_e. In particular, the Mach-5 cases with a colder wall show $2St/C_f \sim 1.35$ for $x > 15\delta_0$, while increasing the wall temperature leads to $2St/C_f \sim 1.3$ in the same region of the computational domain. The cases at Mach 6 show similar values of the Reynolds analogy factor in the preshock and postshock sections of the flow. The introduction of the endothermicity due to the CIG model increases the Reynolds analogy factor for all the analyzed wall-cooling ratios and edge Mach numbers. This effect is more visible in the upstream section of the flows with the warmer wall. This variation of $2St/C_f$ is probably due to the aforementioned difficulties in correctly normalizing the heat flux at the wall in the CIG setups rather than to a change in the flow dynamics.

C. Wall-pressure fluctuations

Figure 8 shows the root-mean-square of the wall-pressure fluctuations induced by the SBLI for the nine computational setups presented in this work. The fluctuation intensity is about 10% of the preshock mean free-stream pressure, up to a distance $2\delta_0$ from the compression corner, as shown by Figs. 8(a), 8(c) and 8(e). Past this location, the pressure fluctuation intensity rises, showing the upstream influence of the SBLI that is generated at the compression corner. The distributions feature a second change in slope around the compression corner, where the growth of the pressure fluctuations becomes steeper for an additional distance $2\delta_0$. The maximum of the pressure fluctuation intensity is then achieved about $5\delta_0$ downstream of the compression corner. The effects of the thermodynamic conditions of the gas on this peak are very similar to those observed for the skin-friction coefficient. In each set of calculations, the low-enthalpy case shows the
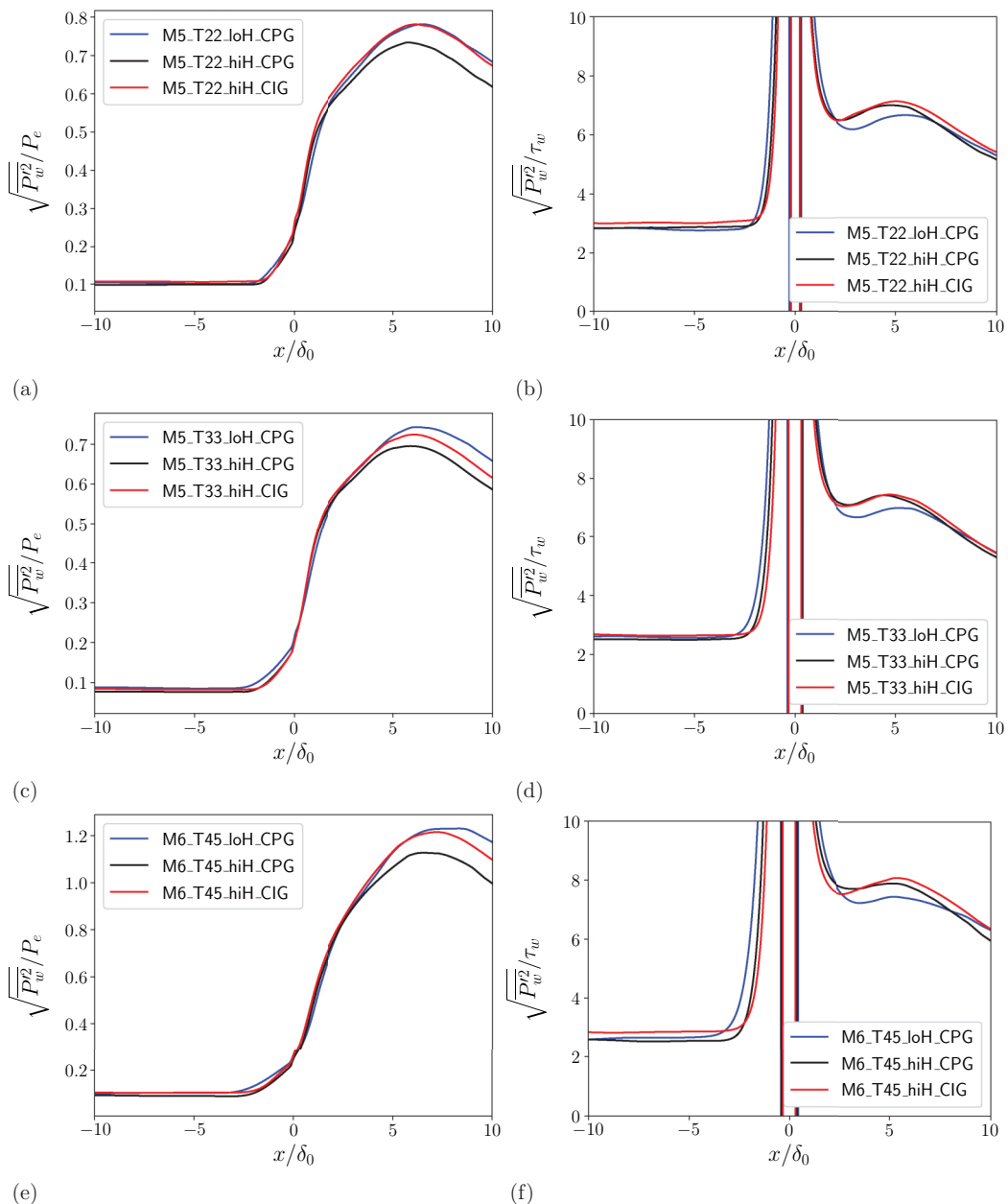
FIG. 8. (a), (b) Streamwise distribution of root-mean-square wall pressure normalized by (a), (c), (e) the free-stream pressure and (b), (d), (f) the local wall-shear stress. Panels (a), (b) refer to the cases at $M_e = 5$ and $T_w/T_e = 2.2$, (c), (d) to the case at $M_e = 5$ and $T_w/T_e = 3.3$, and (e), (f) to the cases at $M_e = 6$ and $T_w/T_e = 4.5$.

strongest pressure fluctuations, the high-enthalpy CPG setup has the weakest pressure fluctuations, and the high-enthalpy CIG case lies in between. The peak pressure fluctuation intensity is usually located at the shock foot in supersonic SBLIs, as the shock motion induces large footprints in terms of wall pressure [22,42,43]. One of the most interesting aspects of the present results is that the strongest pressure fluctuations are not generated by the shock itself. In fact, the peak of pressure

(a)

(b)
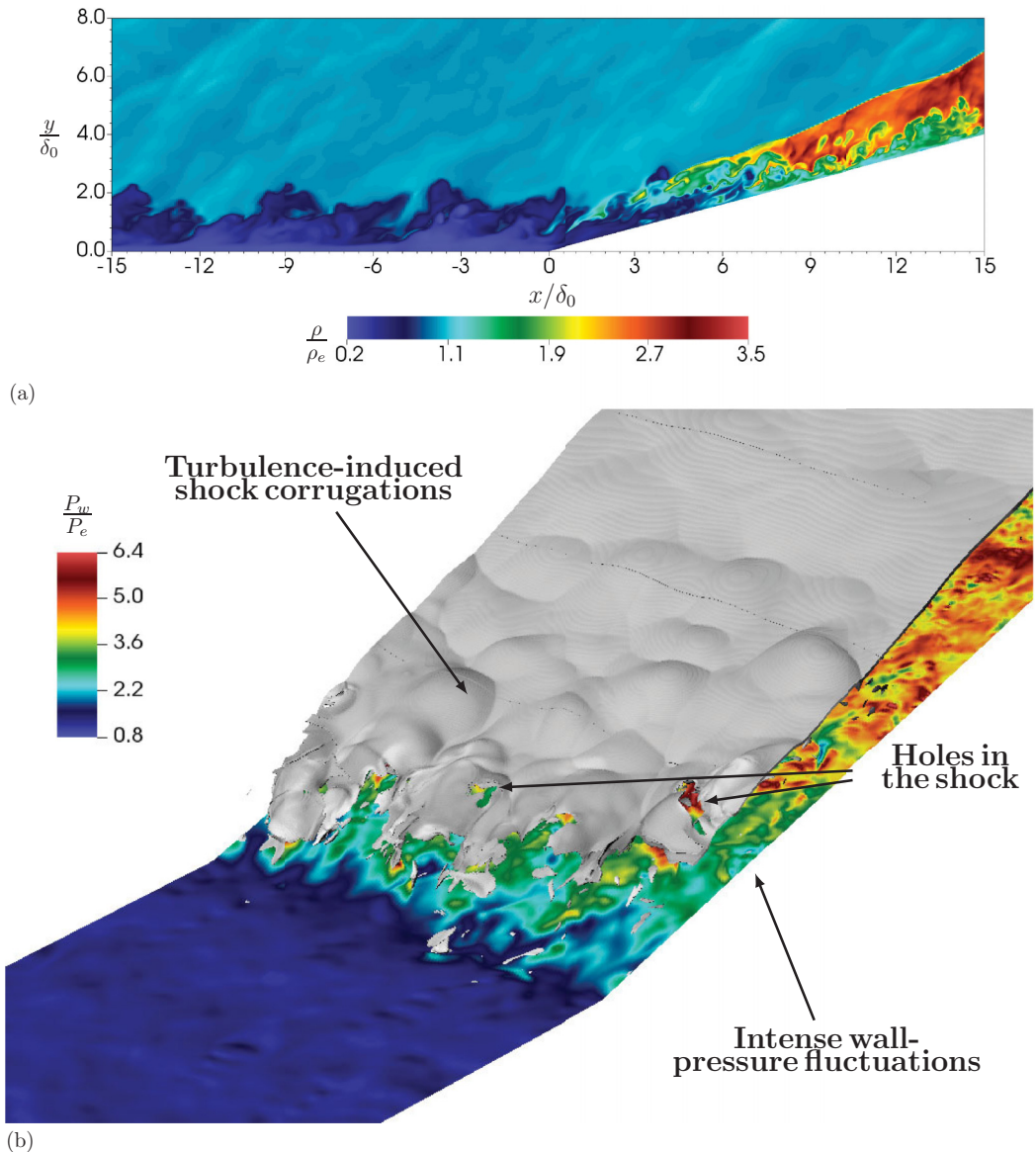
FIG. 9. Instantaneous visualizations of the flow around the compression corner for the case M5_T22_loH_CPG. (a) Contours of density in the x-y plane. (b) Three-dimensional visualization of the instantaneous shock position using a Ducros sensor. The surface of the wall is colored by the local value of the wall pressure normalized by the edge pressure in the preshock conditions.

fluctuations occurs where the large eddies generated in the outer portion of the upstream boundary layer impinge on the shock wave and the ramp following the compression corner, as shown in the instantaneous density contours in Fig. 9(a). In the figure it is possible to observe that large eddies in the outer section of the preshock boundary layer (dark blue regions in the figure) are able to survive the shock and eventually impinge on the surface of the ramp, whereby their momentum locally introduces a large increase in pressure. Figure 9(b) shows that the shock wave, visualized by an isosurface of the Ducros sensor, is severely corrugated by the interaction with these highly

energetic turbulent structures. Note that the presented figure has been obtained by considering the isosurface of the Ducros sensor $\Phi = -\nabla \cdot \mathbf{u}/\sqrt{(\nabla \cdot \mathbf{u})^2 + |\nabla \times \mathbf{u}|^2 + (U_e/\delta_0)^2} = 0.6$; however, identical conclusions could be drawn by using any of the isosurfaces constructed in the interval $0.4 \leqslant \Phi \leqslant 0.7$. The effects of the shock wave and turbulence interaction are visible for several boundary-layer thicknesses downstream of the compression corner in the form of bulges in the shock wave that are advected along the direction of the flow. The intensity of the turbulent fluctuations produced in the upstream boundary layer is high enough to generate holes in the shock wave, locally entering the broken shock regime [44]. Further details about the properties of the shock wave and turbulence interaction are provided in Sec. III F.

D. Spectral properties of wall-pressure fluctuations

The time spectra of the wall-pressure fluctuations are analyzed in this section. The data that are presented focus on the Mach-5 cases with a warmer wall ($T_w/T_e = 3.3$). The results of the cases with stronger wall cooling and higher Mach numbers have been omitted from this analysis because they lead to very similar observations. Figure 10 shows color maps that represent the premultiplied power spectral density of wall pressure throughout the computational domain. The spectra are averaged over the spanwise direction and plotted such that the x axis of the figure corresponds to the stream-wise coordinate of the computational domain and the y axis to Strouhal number $\mathrm{Sr} = f\delta_0/U_e$, where f is the signal frequency. These plots can be divided into three main regions. There is an upstream attached boundary-layer region ($-60\delta_0 < x < -2\delta_0$) where the spectral density is independent of the streamwise location. The power spectral density peaks roughly at $\mathrm{Sr} \sim 0.8$ in this region, which is consistent with the standard behavior of a turbulent boundary layer. The flow separation and reattachment locations correspond to the long tails of the power spectral density shown at $x \sim \pm\delta_0$ in Fig. 10. At these locations the pressure fluctuates on a wide range of time frequencies, which almost spans two orders of magnitude of Strouhal numbers. The structure of the wall-pressure spectra is quickly recovered about $20\delta_0$ downstream of the separation bubble, whereby the most energetic mode in the pressure is again located at about $\mathrm{Sr} \sim 1$. However, the fluctuation spectra are much wider in this postshock region compared to the preshock boundary layer. Figure 11 shows the premultiplied power spectral densities of the wall-pressure signal extracted at four locations along the evolution of the flow. These line plots provide a more quantitative assessment of the differences between the three discussed calculations in the upstream boundary layer, at the compression corner, at $x = 1\delta_0$, and at the location of maximum $\overline{P_w'^2}$. The increase in the stagnation enthalpy of the flow and the introduction of vibrational excitation have the effect of shifting the energy toward higher frequencies. In fact, we can observe that the spectra extracted for M5_T33_loH_CPG are always located at lower frequencies, while M5_T33_hiH_CIG produces the highest frequency signals. The wall-pressure spectra of the case M5_T33_hiH_CPG are located in the middle. The shift between the case M5_T33_hiH_CIG and M5_T33_loH_CPG, which is larger at the compression corner and is mostly negligible at $x = \delta_0$, is a consequence of the local Reynolds number variations discussed in Sec. III A.

E. Proper orthogonal decomposition of the pressure field

This section analyzes the main modes of the pressure field that contribute to the formation of the wall-pressure oscillations discussed so far in this work. This analysis is carried out by performing the proper orthogonal decomposition (POD) of the pressure fluctuations extracted regularly in time on an x-y plane of the flow. The results presented in this section are extracted from the M5_T33_loH_CPG setup, but similar behavior is observed for all the executed calculations. Figure 12(a) shows the cumulative energy of the first 100 POD modes that have been computed. The first 10 POD modes contain roughly 40% of the total energy of the pressure fluctuation signal and specifically, the first six modes are representative of approximately one-third of the overall pressure fluctuation energy. As shown by the power spectra map of the chronomodes in Fig. 12(b), the first
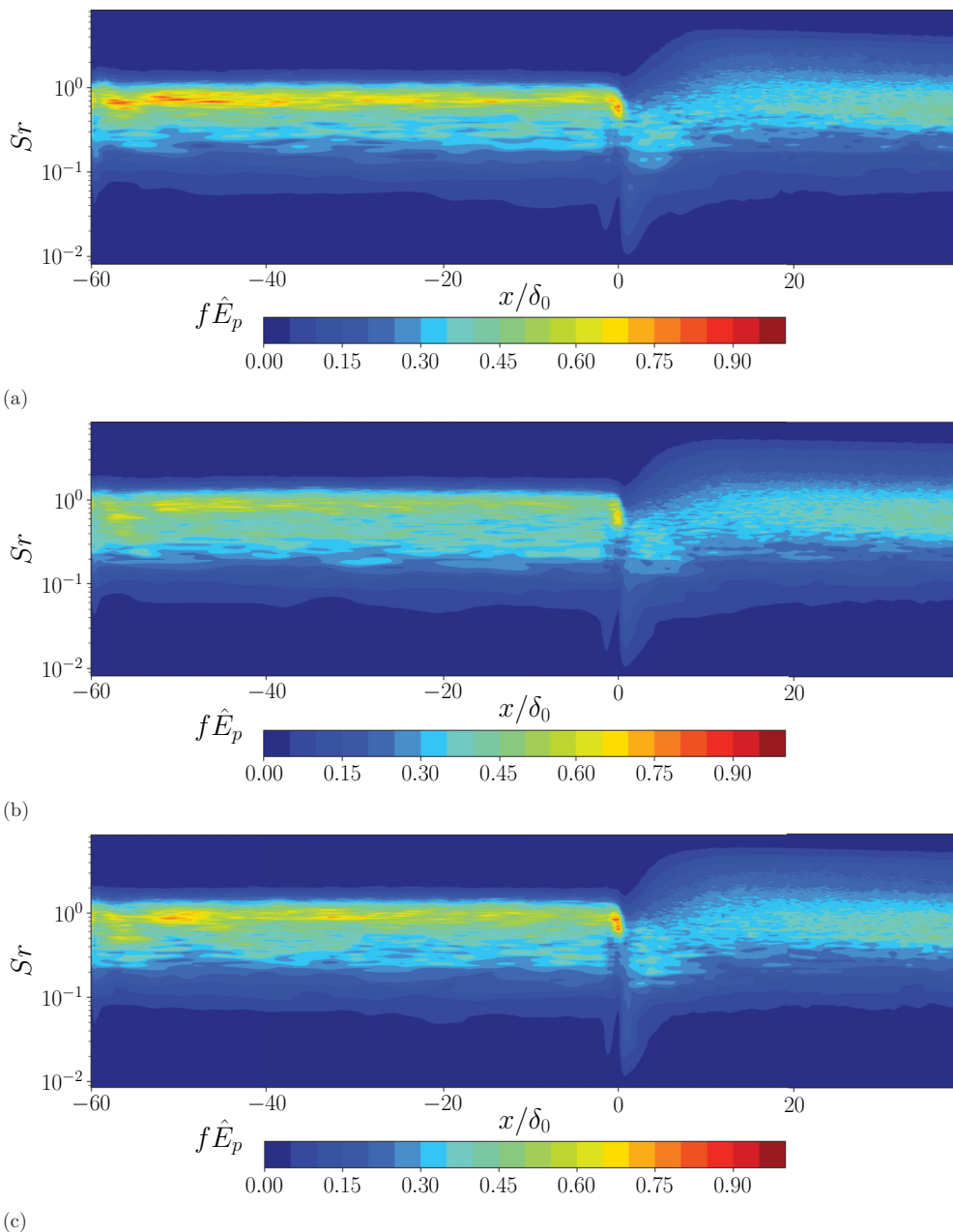
FIG. 10. Premultiplied spectra of the wall pressure for the cases with $T_w/T_e = 3.3$, namely, (a) M5_T33_loH_CPG, (b) M5_T33_hiH_CPG, and (c) M5_T33_hiH_CIG. Instantaneous visualizations of the flow around the compression corner for the case M5_T22_loH_CPG.

five POD modes correspond to relatively high-frequency pressure fluctuations, whose dominant timescale approximately corresponds to Sr ~ 0.1. On the contrary, the sixth POD mode is active on a much lower frequency corresponding to Sr ~ 0.02, which is roughly the lowest frequency observed in Fig. 10. Considering that the sixth mode is clearly the most energetic in that frequency range, it can be identified as the major contributor to the low-frequency oscillations described in
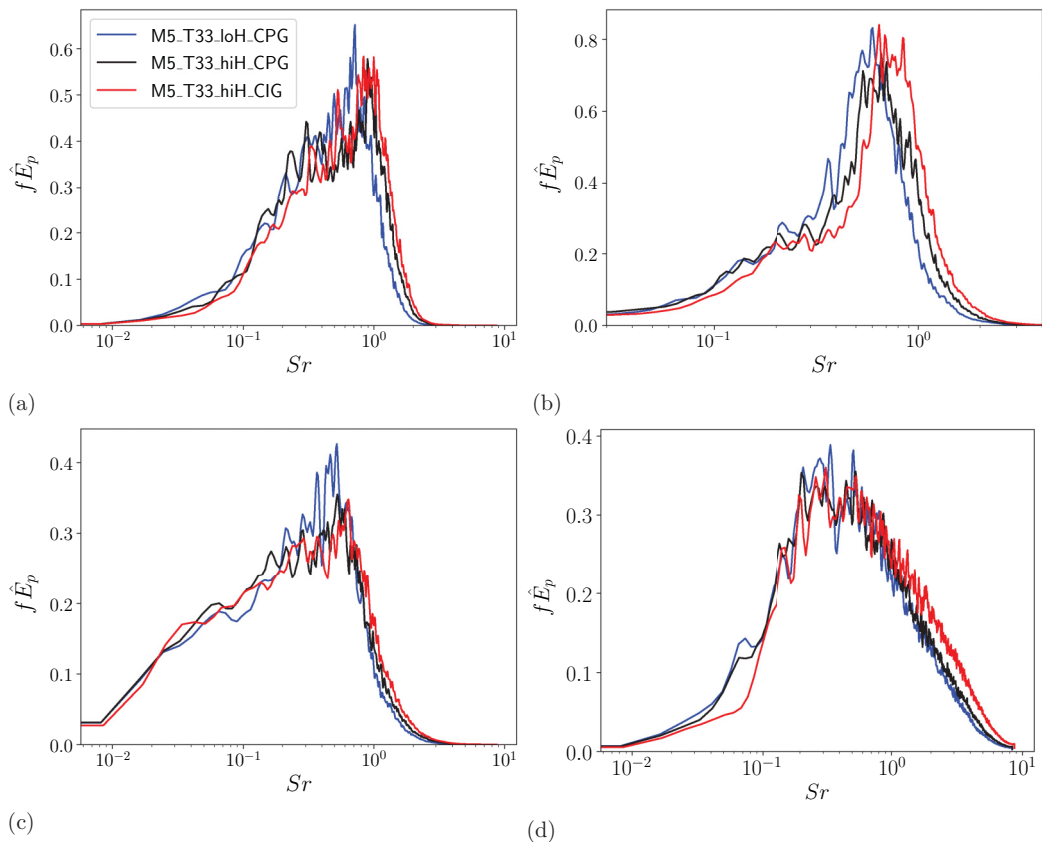
FIG. 11. Premultiplied spectra of the wall pressure for the cases with $T_w/T_e = 3.3$ computed (a) at $x = -10\delta_0$, (b) at the compression corner, (c) at $x = \delta_0$, and (d) at the location of maximum $\overline{P_w'^2}$.

Sec. III D. The first five POD modes correspond to local corrugations of the shock wave, as shown by Figs. 12(c)–12(g). These corrugations, which appear as sinusoidal oscillations localized at the mean shock-wave location in the shown panels, have a significant footprint in the postshock region and toward the wall. In particular, it appears that each of the lobes located on the mean shock line has a tail that elongates toward the wall in the upstream direction. This tail is particularly evident in Fig. 12(e). On the other hand, the sixth POD mode shown in Fig. 12(h) has a completely different shape. It consists of a mode that is constant along the shock wave and represents a breathing motion of the discontinuity that rigidly moves upstream and downstream with respect to the compression corner. Each rigid motion upstream (downstream) of the shock generates an approximately uniform decrease (increase) of the pressure in the postshock region. For this reason, the results of the POD analysis suggest that the high-frequency wall-pressure oscillations observed in the previous section are due to corrugations of the shock wave, while the mild low-frequency oscillations are induced by the breathing motion of the shock wave.

F. Shock wave and turbulence interaction

The description of the turbulent boundary layer performed in Sec. III A highlights that the considered flows upstream of the compression corner are mostly independent of the stagnation enthalpy or thermodynamic model that is considered in the calculation. Thus, the reasons for the pressure variance modifications at the wall analyzed in Sec. III C must be sought in the modification
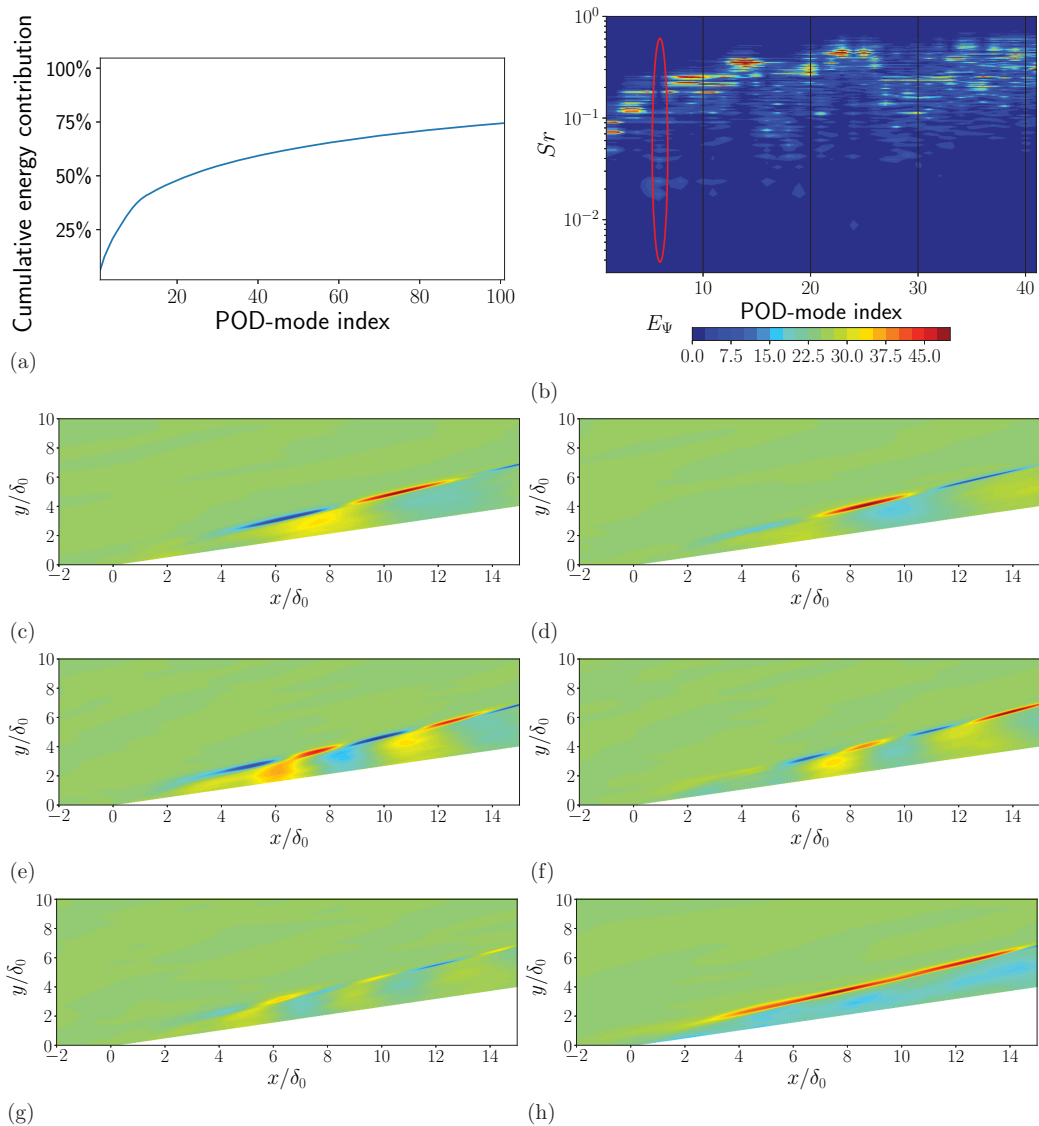
FIG. 12. (a) Cumulative energy contribution on the first 100 POD modes for the M5_T33_loH_CPG case. (b) Power spectral density of the first 40 most energetic chronomodes. (c)–(h) The shape of the first six POD modes ordered by energy content for the M5_T33_loH_CPG case. The red ellipse in panel (b) highlights the power spectrum of the sixth chronomode.

of the shock wave and turbulence interaction in the vicinity of the compression corner. Figure 13 shows the profiles of turbulent Mach number $M_t = \sqrt{\widetilde{u_i'' u_i''}}/\overline{a}$ extracted just after the compression corner ($x = 5\delta_0$) where the outer part of the incoming boundary layer interacts with the oblique shock. These profiles are characterized by a plateau that extends between $y^* \sim 10$ and $y^* \sim 100$, whereby $M_t \sim 0.55$ for the Mach-5 cases and $M_t \sim 0.65$ for the Mach-6 cases. The considered compression ramp produces a shock wave inclined by about $24°$ and $22°$ in the Mach-5 and Mach-6 cases, respectively. In these conditions, the normal Mach number of the upstream flow with respect to the undisturbed shock wave is about 2.0 and 2.3, respectively. Larsson *et al.* [44] and Donzis
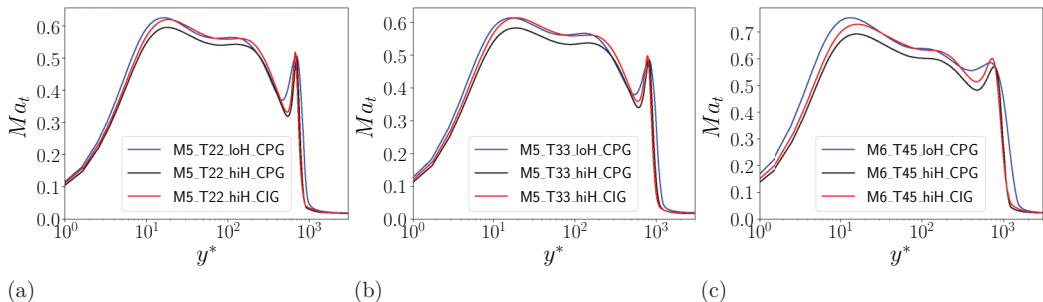
FIG. 13. Turbulent Mach-number profiles at $x = 5\delta_0$ for the cases (a) $M_e = 5$ and $T_w/T_e = 2.2$, (b) $M_e = 5$ and $T_w/T_e = 3.3$, and (c) $M_e = 6$ and $T_w/T_e = 4.5$.

[45] have found that a planar-shock-wave and isotropic-turbulence interaction transitions from a wrinkled shock regime, whereby the shock is only corrugated by the preshock turbulence, to a broken shock regime, where the thermodynamic fluctuations of the incoming turbulence are so strong as to generate holes in the shock when $M_t \gtrsim 0.6(M_n - 1)$, where M_n is the convective Mach number of the flow normal to the shock wave. While keeping in mind that this approximate relation has only been verified for homogeneous isotropic turbulence and that the turbulence generated by the precompression corner boundary layer is far from being isotropic and homogeneous, it is interesting that the values of M_t observed in these calculations marginally satisfy the inequality above and suggest a broken shock condition. Considering that holes in the shock have been visualized for the computed cases, for example, in Fig. 9, it is possible to suggest that the inequality above could be sufficiently robust to describe the transition from wrinkled to broken regimes, even in the case of oblique shocks interacting with inhomogeneous and anisotropic turbulence. Clearly, this initial piece of evidence does not provide definitive proof of this theory, which will require further investigation to be verified.

Another interesting aspect that emerges from the graphs in Fig. 13 is the correlation between the levels of M_t and the peak of wall-pressure variance shown in Fig. 8. In fact, it appears that in all the examined conditions, the low-enthalpy CPG calculations are characterized by the highest turbulent Mach number; the high-enthalpy CPG configurations have the lowest turbulent Mach number; and the high-enthalpy CIG flows have intermediate values of M_t, which are most of the times closer to the low-enthalpy profiles. The similarity of the enthalpy effects on this quantity with the variations described in Sec. III C, together with the results of the POD analysis in Sec. III E and the strong shock corrugation highlighted in Fig. 9, suggests that the analyzed pressure fluctuations at the wall are the direct footprint of the oblique-shock-wave and turbulent interaction that happens just above the compression ramp. At high turbulent Mach numbers, any oscillation of the thermofluid-dynamic quantities in the preshock turbulent boundary layer will induce a local modification of the oblique shock wave with a consequent variation of the local momentum of the flow in the normal direction to the compression ramp wall.

IV. CONCLUSIONS

DNSs of turbulent boundary layers flowing over a $15°$ compression ramp have been carried out in this study. The presented calculations consider two upstream-edge Mach numbers, namely, 5 and 6, two rates of wall cooling, and two levels of stagnation enthalpy. The lowest stagnation enthalpy is representative of the state of the art of hypersonic turbulence simulations, and it considers a flow with a free-stream temperature of 100 K that remains in the CPG regime throughout the computational domain. The highest stagnation enthalpy corresponds to a free-stream temperature of 500 K, which is sufficiently high to allow the gas molecules to become vibrationally excited within the turbulent boundary layer formed over the compression ramp and across the ramp-induced

shock wave. However, the maximum gas temperature encountered in all these cases always remains sufficiently low to warrant marginal activation of other high-temperature effects, such as chemical dissociation.

The presented results have shown that an increase in the stagnation enthalpy decreases the skin-friction coefficient, the Stanton number, and the wall-pressure fluctuations by about 10% while retaining the CPG assumption. Introducing the endothermic effects associated with vibrational excitation partially compensates for this decrease, yielding values of the normalized mechanical and thermal stresses at the wall that are halfway between the low-enthalpy and high-enthalpy calorically perfect flow solutions. However, a different normalization of the heat flux, which does not take into account the nonlinear relation that exists between temperature and enthalpy in the CIG model, shows that vibrational excitation actually decreases the heat flux at the wall by about 20%. The conflicting conclusions offered by two normalizations prompt further investigation into the correct scaling for this quantity. Another effect associated with stagnation enthalpy variation which has some engineering relevance is the shift of the wall-pressure fluctuations toward higher frequencies. In fact, the increase in stagnation enthalpy in the CPG simulation and the introduction of vibrational excitation increase the peak frequency of pressure fluctuations at the compression corner. Considering that the most energetic frequency shifts by a factor of 2 between the low-enthalpy and high-enthalpy vibrationally excited flow, it appears that high-enthalpy effects should be taken into account when dynamical loads generated by this type of flow are evaluated. In the context of describing the pressure fluctuation field, it has been shown using POD analysis that the most energetic low-frequency modes of the wall pressure are associated with a breathing motion of the oblique shock induced by the compression corner, while the high-frequency pressure fluctuations are instead due to the shock corrugation generated by the highly compressible turbulence that impinges on the shock wave.

The results reported in this study provide an initial assessment of the importance of high-enthalpy effects in the prediction of hypersonic wall-bounded turbulence and, in particular, of hypersonic shock wave and turbulent boundary-layer interactions. However, the flow conditions under scrutiny here are at the lower end of the hypersonic regime, and the free-stream enthalpy is such that only vibrational excitation is triggered. Future work will focus on verifying the conclusions of this study for flows at higher Mach numbers and higher enthalpy in which chemical and thermal nonequilibrium effects play a role.

APPENDIX: VERIFICATION USING A SUPERSONIC COMPRESSION CORNER

This Appendix provides a verification of the formulation deployed to obtain the presented results with a Mach-2.9 turbulent compression corner flow. In particular, the flow configuration presented and discussed by Wu and Martin [46] has been selected for this verification. A Mach-2.9 turbulent boundary layer, whose free-stream temperature is 107.1 K, flows over a $24°$ compression corner that is kept at $T_w = 307$ K. The Reynolds number based on the momentum thickness of the incoming boundary layer is $Re_\theta = 2300$ at the location $x = 9\delta_0$, whereby δ_0 is the boundary-layer
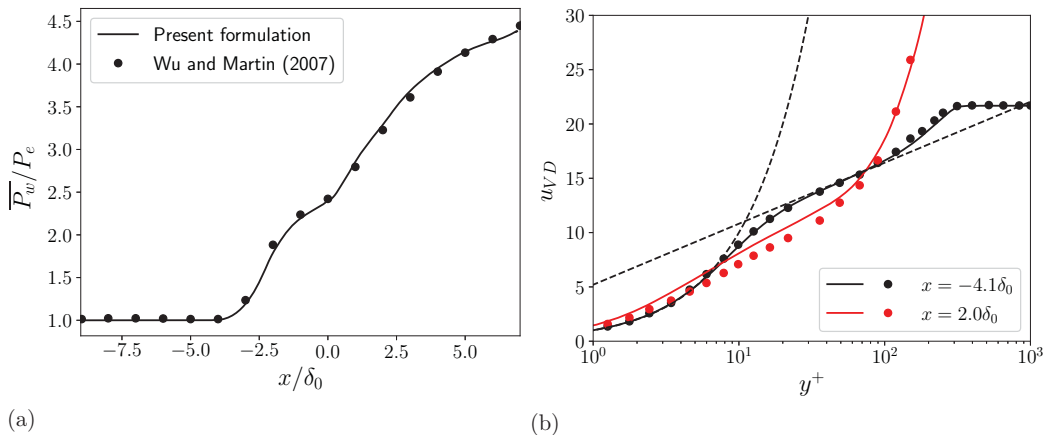
FIG. 14. Verification of the (a) streamwise distribution of mean pressure and (b) wall-normal van Driest–transformed velocity profiles obtained upstream ($x = -4.1\delta_0$) and downstream ($x = 2\delta_0$) of the compression corner. The solid lines correspond to the results of the present formulation while the symbols to the results of Wu and Martin [46].

thickness at the same location. The calculations presented in this section are executed with the same methodology described in Sec. II, except for (i) the computational domain is significantly smaller, namely, $L_1 = 29\delta_0$, $L_2 = 9\delta_0$, the height of the domain is $5\delta_0$, and its width is $2.6\delta_0$; (ii) the sampling station for the recycle-rescaling location is positioned at $x = -20\delta_0$; (iii) the computational deployed computational grid consists of $2800 \times 256 \times 192$ points in the streamwise, wall-normal, and spanwise directions, respectively. Note that the computational domain utilized in this verification is significantly longer than the original domain utilized by Wu and Martin [46]. Such a modification of the computational domain has been dictated by the will of reducing the influence of the inflow boundary conditions on the compression corner flow.

Figure 14 shows a comparison of the results obtained with the present formulation and those provided by Wu and Martin [46]. The agreement is within plotting accuracy for both the wall-pressure profiles and the upstream velocity profile. Minor discrepancies are observed for the near-wall section of the van Driest transformed velocity profile extracted just downstream of the interaction at $x = 2\delta_0$. Considering the small deviation of the velocity profiles in this section and the overall agreement of the other quantities, the presented results provide a successful verification of the numerical methodology.

[1] J. D. Anderson, Jr., *Hypersonic and High-Temperature Gas Dynamics*, 3rd ed. (AIAA Press, Reston, VA, 2006).

[2] I. A. Leyva, The relentless pursuit of hypersonic flight, Phys. Today **70**, 30 (2017).

[3] J. Urzay, Supersonic combustion in air-breathing propulsion systems for hypersonic flight, Annu. Rev. Fluid Mech. **50**, 593 (2018).

[4] G. V. Candler, Rate effects in hypersonic flows, Annu. Rev. Fluid Mech. **51**, 379 (2019).

[5] M. Bernardini and S. Pirozzoli, Wall pressure fluctuations beneath supersonic turbulent boundary layers, Phys. Fluids **23**, 085102 (2011).

[6] C. Wenzel, T. Gibis, and M. Kloker, About the influences of compressibility, heat transfer and pressure gradients in compressible turbulent boundary layers, J. Fluid Mech. **930**, A1 (2022).

[7] M. P. Martin, Direct numerical simulation of hypersonic turbulent boundary layers, Part 1. Initialization and comparison with experiments, J. Fluid Mech. **570**, 347 (2007).

[8] L. Duan, I. Beekman, and M. P. Martin, Direct numerical simulation of hypersonic turbulent boundary layers, Part 2. Effect of wall temperature, J. Fluid Mech. **655**, 419 (2010).

[9] L. Duan and M. P. Martin, Direct numerical simulation of hypersonic turbulent boundary layers, Part 4. Effect of high enthalpy, J. Fluid Mech. **684**, 25 (2011).

[10] C. Zhang, L. Duan, and M. M. Choudhari, Direct numerical simulation database for supersonic and hypersonic turbulent boundary layers, AIAA J. **56**, 4297 (2018).

[11] M. Cogo, F. Salvadore, F. Picano, and M. Bernardini, Direct numerical simulation of supersonic and hypersonic turbulent boundary layers at moderate-high Reynolds numbers and isothermal wall condition, J. Fluid Mech. **945**, A30 (2022).

[12] A. Trettel and J. Larsson, Mean velocity scaling for compressible wall turbulence with heat transfer, Phys. Fluids **28**, 026102 (2016).

[13] P. S. Volpiani, P. S. Iyer, S. Pirozzoli, and J. Larsson, Data-driven compressibility transformation for turbulent wall layers, Phys. Rev. Fluids **5**, 052602(R) (2020).

[14] K. P. Griffin, L. Fu, and P. Moin, Velocity transformation for compressible wall-bounded turbulent flows with and without heat transfer, Proc. Natl. Acad. Sci. USA **118**, e2111144118 (2021).

[15] Y. Fan, W. Li, and S. Pirozzoli, Decomposition of the mean friction drag in zero-pressure-gradient turbulent boundary layers, Phys. Fluids **31**, 086105 (2019).

[16] A. Kianfar, M. Di Renzo, C. T. Williams, A. Elnahhas, and P. L. Johnson, Angular momentum and moment of enthalpy integral equations for compressible boundary layers, Phys. Rev. Fluids **8**, 054603 (2023).

[17] S. Pirozzoli and M. Bernardini, Direct numerical simulation database for impinging shock wave/turbulent boundary-layer interaction, AIAA J. **49**, 1307 (2011).

[18] P. S. Volpiani, M. Bernardini, and J. Larsson, Effects of a nonadiabatic wall on hypersonic shock/boundary-layer interactions, Phys. Rev. Fluids **5**, 014602 (2020).

[19] D. V. Gaitonde, Progress in shock wave/boundary layer interactions, Prog. Aerosp. Sci. **72**, 80 (2015).

[20] S. Priebe and M. P. Martin, Turbulence in a hypersonic compression ramp flow, Phys. Rev. Fluids **6**, 034601 (2021).

[21] M. C. Adler and D. V. Gaitonde, Dynamics of strong swept-shock/turbulent-boundary-layer interactions, J. Fluid Mech. **896**, A29 (2020).

[22] A. Ceci, A. Palumbo, J. Larsson, and S. Pirozzoli, On low-frequency unsteadiness in swept shock wave-boundary layer interactions, J. Fluid Mech. **956**, R1 (2023).

[23] M. Di Renzo and J. Urzay, Direct numerical simulation of a hypersonic transitional boundary layer at suborbital enthalpies, J. Fluid Mech. **912**, A29 (2021).

[24] D. Passiatore, L. Sciacovelli, P. Cinnella, and G. Pascazio, Thermochemical non-equilibrium effects in turbulent hypersonic boundary layers, J. Fluid Mech. **941**, A21 (2022).

[25] D. Passiatore, L. Sciacovelli, P. Cinnella, and G. Pascazio, Shock impingement on a transitional hypersonic high-enthalpy boundary layer, Phys. Rev. Fluids **8**, 044601 (2023).

[26] M. Di Renzo, L. Fu, and J. Urzay, HTR solver: An open-source exascale-oriented task-based multi-GPU high-order code for hypersonic aerothermodynamics, Comput. Phys. Commun. **255**, 107262 (2020).

[27] M. Di Renzo and S. Pirozzoli, HTR-1.2 solver: Hypersonic task-based research solver version 1.2, Comput. Phys. Commun. **261**, 107733 (2021).

[28] M. Di Renzo, HTR-1.3 solver: Predicting electrified combustion using the hypersonic task-based research solver, Comput. Phys. Commun. **272**, 108247 (2022).

[29] B. J. McBride, M. J. Zehe, and S. Gordon, NASA/TP-2002-211556, Tech. Rep. (NASA, 2002).

[30] S. Pirozzoli, Stabilized non-dissipative approximations of Euler equations in generalized curvilinear coordinates, J. Comput. Phys. **230**, 2997 (2011).

[31] S. Pirozzoli, Generalized conservative approximations of split convective derivative operators, J. Comput. Phys. **229**, 7180 (2010).

[32] L. Fu, X. Y. Hu, and N. A. Adams, A family of high-order targeted ENO schemes for compressible-fluid simulations, J. Comput. Phys. **305**, 333 (2016).

[33] C. T. Williams, M. Di Renzo, and P. Moin, *Center for Turbulence Research, 203 Annual Research Briefs*, Tech. Rep. (Center for Turbulence Research, Stanford, 2022).

[34] S. Gottlieb, C.-W. Shu, and E. Tadmor, Strong stability-preserving high-order time discretization methods, SIAM Rev. **43**, 89 (2001).

[35] T. S. Lund, X. Wu, and K. D. Squires, On the generation of turbulent inflow conditions for boundary layer simulations, J. Comput. Phys. **140**, 233 (1998).

[36] T. J. Poinsot and S. K. Lele, Boundary conditions for direct simulations of compressible viscous flows, J. Comput. Phys. **101**, 104 (1992).

[37] J. Urzay and M. Di Renzo, *Center for Turbulence Research Annual Research Briefs*, Tech. Rep. (Center for Turbulence Research, Stanford, 2020).

[38] E. R. van Driest, The problem of aerodynamic heating, Aeronaut. Eng. Rev. **15**, 26 (1956).

[39] Y. S. Zhang, W. T. Bi, F. Hussain, and Z. S. She, A generalized Reynolds analogy for compressible wall-bounded turbulent flows, J. Fluid Mech. **739**, 392 (2014).

[40] K. P. Griffin, L. Fu, and P. Moin, Near-wall model for compressible turbulent boundary layers based on an inverse velocity transformation, J. Fluid Mech. **970**, A36 (2023).

[41] F. M. White, *Viscous Fluid Flow*, 2nd ed. (McGraw-HiII, New York, 1992).

[42] M. Di Renzo, N. Oberoi, J. Larsson, and S. Pirozzoli, Crossflow effects on shock wave/turbulent boundary layer, Theor. Comput. Fluid Dyn. **36**, 327 (2022).

[43] J. Larsson, V. Kumar, N. Oberoi, M. Di Renzo, and S. Pirozzoli, Large-eddy simulations of idealized shock/boundary-layer with crossflow, AIAA J. **60**, 2767 (2022).

[44] J. Larsson, I. Bermejo-Moreno, and S. K. Lele, Reynolds- and Mach-number effects in canonical shock-turbulence interaction, J. Fluid Mech. **717**, 293 (2013).

[45] D. A. Donzis, Shock structure in shock-turbulence interactions, Phys. Fluids **24**, 126101 (2012).

[46] M. Wu and M. P. Martin, Direct numerical simulation of supersonic turbulent boundary layer over a compression ramp, AIAA J. **45**, 879 (2007).